Journal of
Composites Science

MDPI

*Article*

# High-Cycle Fatigue Behaviour and Structural Robustness of Glass Fibre-Reinforced Polymer Tiled Web-Core Sandwich Panel Unit Cells in Load-Bearing Structures

**Jordi Uyttersprot [1], Wouter De Corte [1,*] and Wim Van Paepegem [2]**

[1] Department of Structural Engineering and Building Materials, Faculty of Engineering and Architecture, Ghent University, Tech Lane 60, 9000 Ghent, Belgium; jordi.uyttersprot@ugent.be
[2] Department of Materials, Textiles and Chemical Engineering, Faculty of Engineering and Architecture, Ghent University, Tech Lane 46, 9000 Ghent, Belgium; wim.vanpaepegem@ugent.be
* Correspondence: wouter.decorte@ugent.be

**Abstract:** This paper explores the fatigue behaviour and robustness of tiled web-core sandwich panels used in glass fibre-reinforced polymer bridges, which are increasingly favoured for their lightweight and corrosion-resistant properties. Fatigue tests are conducted on unit cell specimens with manually induced crack initiation, simulating accidental damage scenarios in glass fibre-reinforced polymer bridge components. The objective is to assess the integrity of individual unit cells when subjected to a localized force at the top flange after damage initiation. The fatigue tests reveal three phases in the behaviour of a tiled unit cell. Initially, there is a substantial rapid stiffness degradation with crazing crack appearance within the cross-section. Subsequently, a plateau phase occurs, with limited stiffness degradation and stable crazing cracks, the duration of which depends on the applied fatigue load. Lastly, rapid stiffness degradation with substantial crack growth leads to ultimate failure within roughly a thousand cycles. Further analysis using digital image correlation reveals strain concentrations at the location of crazing cracks and crack propagation occurring interlaminarly but not through the plies of the top and bottom flanges, ensuring a robust design. This research enhances the understanding of the tiled sandwich panels, offering prospects for resilient load-bearing structures in glass fibre-reinforced polymer bridges and structural engineering applications.

**Keywords:** fatigue behaviour; tiled sandwich panels; robustness; load-bearing structures



**Citation:** Uyttersprot, J.; De Corte, W.; Van Paepegem, W. High-Cycle Fatigue Behaviour and Structural Robustness of Glass Fibre-Reinforced Polymer Tiled Web-Core Sandwich Panel Unit Cells in Load-Bearing Structures. *J. Compos. Sci.* **2024**, *8*, 538. https://doi.org/10.3390/jcs8120538

Academic Editors: Xiangfa Wu and Oksana Zholobko

Received: 26 September 2024
Revised: 1 December 2024
Accepted: 13 December 2024
Published: 17 December 2024



## 1. Introduction

The pursuit of lightweight and resilient structural materials has inspired innovations in composite materials [1–5], especially in fields where strength, durability, and damage tolerance are critical [6–10]. Among these materials, tiled sandwich unit cell panels have emerged as a promising contender, holding the potential to provide both structural resilience and weight efficiency [11].

The majority of foot and road bridges constructed with glass fibre-reinforced polymer (GFRP) utilize the web-core sandwich design [12–14]. This design differs from traditional GFRP sandwich panels, which consist of GFRP top and bottom flanges separated by a single lightweight core material panel to enhance structural integrity. Instead, the innovative approach here is the use of a tiled web-core sandwich panel, which incorporates individual foam blocks placed side by side. Fabric plies are draped from the top flange, down between the foam blocks, and then to the bottom flange, effectively connecting both flanges. After resin infusion and curing, these strips between the top and bottom flanges create solid longitudinal laminate stiffeners within the foam core, often referred to as "webs" in analogy to I-profiles. This novel composite concept is termed a tiled sandwich (TS) [15].

The key innovation in the TS concept lies in its ability to prevent flange-core delamination after accidental damage. This is achieved by the fibre reinforcement perpendicular to the direction of crack propagation, rendering it a robust FRP sandwich concept [16]. In contrast, traditional sandwich panels, and even plane-parallel web-core sandwich panels, which feature flanges with a plane-parallel (PP) build-up, can experience a rapid transverse propagation of apparent 3D cracks due to the absence of fibre reinforcement perpendicular to the propagation direction. With the integration of tiled reinforcement in both the core and flanges, a plate material is formed at the top and bottom flanges where the reinforcement is oriented at a slight angle rather than being parallel to the outer surfaces. This stacking is referred to as a tiled laminate (TL), as opposed to PP. In a cross-section, the various plies of reinforcement are of limited width, partially overlap, and are interconnected through suitable resin. The material offers two significant advantages: robustness and modularity. They can both be summarized as follows:

1. Robustness: Robustness is an essential requirement for structural applications, ensuring that a structure is designed and executed in a manner that prevents disproportionate damage caused by events such as explosions, impacts, or human errors [10]. Given the collapses of various bridges worldwide, likely due to the failure of a single structural element, the need for robustness is self-evident.
2. Modularity: The concept's modularity allows for the production of composite plates from tiled fabric strips, facilitating the robotized manufacturing of large construction panels of varying shapes and sizes. It also has applications in producing wrinkling-proof double-curved laminates in shipbuilding and facade elements, as well as components for complex, one-of-a-kind offshore structures. Its versatility spans bridge decks, lock gates, wall and floor panels, and blast protection systems.

In addition to examining the static transverse mechanical properties of these TSs [17–24], it is imperative to devote special attention to fracture mechanics and fatigue crack growth, as these factors significantly influence robustness [21–24]. In conventional PP composites, interlaminar cracks can originate from the laminate's free edges or internally due to factors such as accidental impacts. However, in a tiled laminate structure, there is an abundance of ply edges, both at the free edges and regularly spaced along the top and bottom flanges, positioned at a slight angle relative to the top and bottom surfaces.

The primary objective of this study is to evaluate the transverse robustness of an individual unit cell within a tiled sandwich structure, specifically its ability to contain and limit the spread of accidental damage within the cell itself. This robustness assessment is conducted in the context of the interactions between neighbouring unit cells, with a focus on structural responses under localized force applications at the top flange following the initiation of damage. Understanding the fatigue behaviour and crack evolution in these tiled sandwich unit cell panels is critical, as it provides insight into the structural integrity and durability of tiled sandwich composites under cyclic loading.

The outcomes of this research carry significant implications for engineering applications, particularly in sectors requiring high-strength, damage-tolerant materials, such as bridge construction and other critical load-bearing structures. By investigating how these unit cells respond to damage and fatigue, this study aims to contribute to the design and optimization of robust composite structures that can withstand demanding operational conditions.

Following this introduction, Section 2 discusses the static three-point bending (3PB) test to failure for unit cell specimens with and without foam cores. Next, Section 3 provides an overview of the fatigue specimens and setup. The results of the static 3PB test are then used to determine the fatigue load in Section 4. Section 5 presents the results of the fatigue tests for different load levels, supplemented with an analysis of the stiffness degradation during the fatigue test. In this part, the 3D strain field of the critical flange–web connection is also studied using DIC imaging together with an analysis of the fracture behaviour using online microscopy during the fatigue tests. Finally, the most important conclusions are listed in Section 6.

## 2. Static Three-Point Bending Test

This study employs the ASTM D7264 standard procedure A [25] for a 3PB test on a unit cell specimen to assess the flexural strength and stiffness properties of continuous-fibre-reinforced polymer matrix composites. This method utilizes a three-point loading system, with a centre load applied on a simply supported beam. In this configuration, the maximum flexural stress is situated directly under the centre loading nose, resulting in a linear vertical shear force distribution over the entire specimen. Notably, while [25] is designed for testing GFRP laminate with a span-to-thickness ratio of 32:1, some aspects of the standard are adapted for the 3PB test in this section. For instance, the authors carefully selected the test setup and specimen dimensions to gain valuable insights into the critical mechanical properties of the typical web-core sandwich panel bridges.

Two unit cell cross-sections, one with foam and one without foam cores, are extracted from the web-core bridge deck panel. These specimens have identical dimensions: a total width of 811 mm, a height of 250 mm, average web thicknesses of 7 mm, and a centre-to-centre distance between the webs of 100 mm. The specimens undergo a slightly asymmetrically loaded 3PB test, with the loading nose approximately 550 mm from the left side of the unit cell specimen and a span length between the supports of 600 mm. Figure 1 provides an overview of the two distinct test setups, each denoted by abbreviations indicating the presence (F) or absence (nF) of foam blocks and the asymmetric (A) load case.

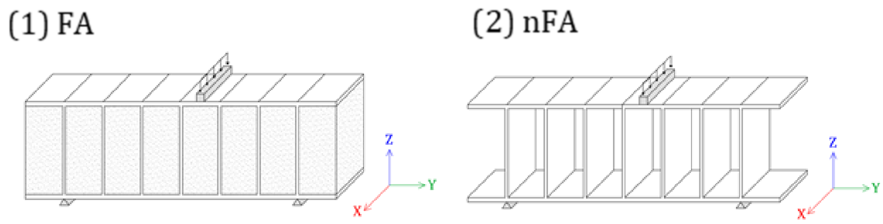


**Figure 1.** Asymmetric 3PB test setups with and without foam cores.

The tests involve applying a force to the specimen with a crosshead movement rate of 3.0 mm/min while measuring and recording the resulting specimen deflection by dial gauges at mid-span until failure occurs in the top flange and/or bottom flange and the applied force. To prevent damage to the dial gauges upon specimen failure, deflection measurement employs a cantilevered steel plate fixed to the underside of the bottom flange. Additionally, dial gauges are positioned at the top and bottom of the steel plate to account for deformations of the steel plate itself. These dial gauges measure the relative deflection ($w_{rel}$) of the bottom flange, which is calculated as the difference between the imposed displacement by the plunger ($w_{imp}$) and the actual deflection ($w_{act}$) (see Figure 2). Given the assumption of a sufficiently rigid test setup frame and a constant distance between the top and bottom flanges at the loading point, the measured differential deflection reflects local compressions at the support and loading nose locations.

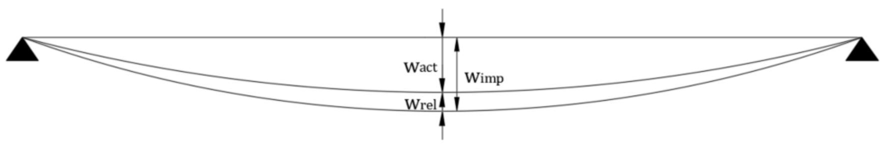


**Figure 2.** Measured relative deflection as the difference between the imposed and actual deflection in a 3PB test setup with centre dial gauges.

The unit cell specimens, both with and without foam blocks, undergo an asymmetric loading between two webs until the ultimate failure event. Figures 3 and 4 present the force–deflection results of the 3PB tests for the samples with and without foam, respectively. In these graphs, local failure events within the unit cell specimen are marked and numbered, in accordance with Figure 5 for the unit cell with foam and Figure 6 for the unit cell without foam. Tables 1 and 2, situated below the graphs, provide the associated deflection and applied force values along with a description of the failure mechanisms for different local failure events during the 3PB test of the unit cell, organized according to field numbers from left to right.

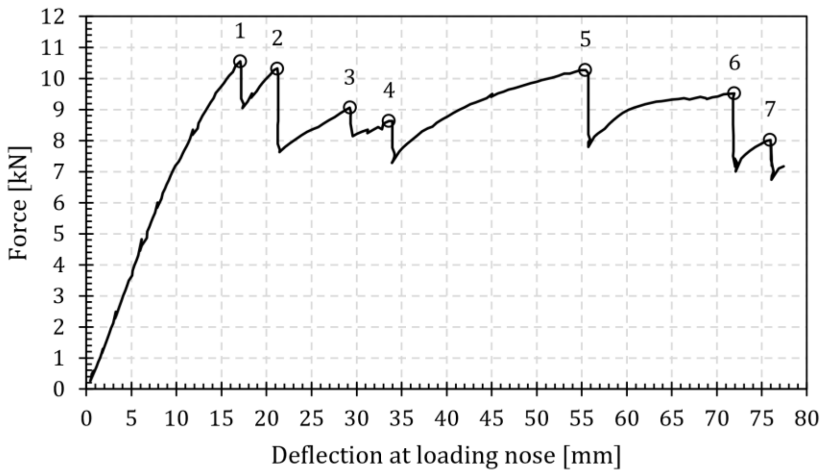


**Figure 3.** Force–deflection graph for an asymmetrically loaded unit cell specimen with foam inserts until ultimate failure.

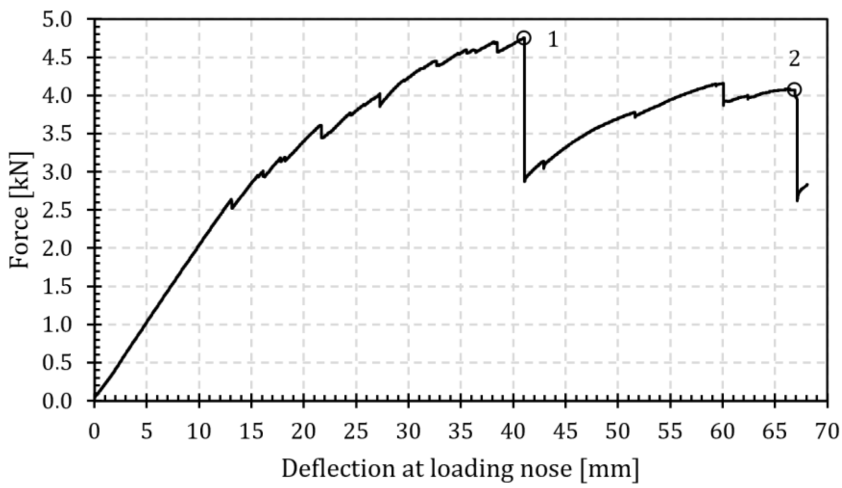


**Figure 4.** Force–deflection graph for an asymmetrically loaded unit cell specimen without foam inserts until ultimate failure.

For the unit cell with foam cores, the initial ply failure occurs at the bottom flange, with a deflection of 29.25 mm and a force of 9.06 kN. This event entails the delamination of a ply end under tensile stresses in the lower flange. Subsequently, ultimate failure is marked by a second delamination of the bottom flange, at a deflection of 75.94 mm and a force of 8.02 kN. Additionally, localized delaminations occur in the top flange due to compressive stresses, but these do not propagate further to the top of the top flange.

In contrast, in the absence of foam cores, the initial ply failure of the unit cell specimen manifests at a significantly larger deflection and lower force. The failure behaviour is also distinct from the specimen with foam, with the first ply failure occurring in the top flange within the loaded field on the left side of the load. In this scenario, the crack is constrained by the presence of a transverse 90° ply wrapped around the foam cores. Ultimate failure entails the delamination of a free-ply end in the bottom flange, similar to the specimen with foam, albeit with smaller deformations and forces.

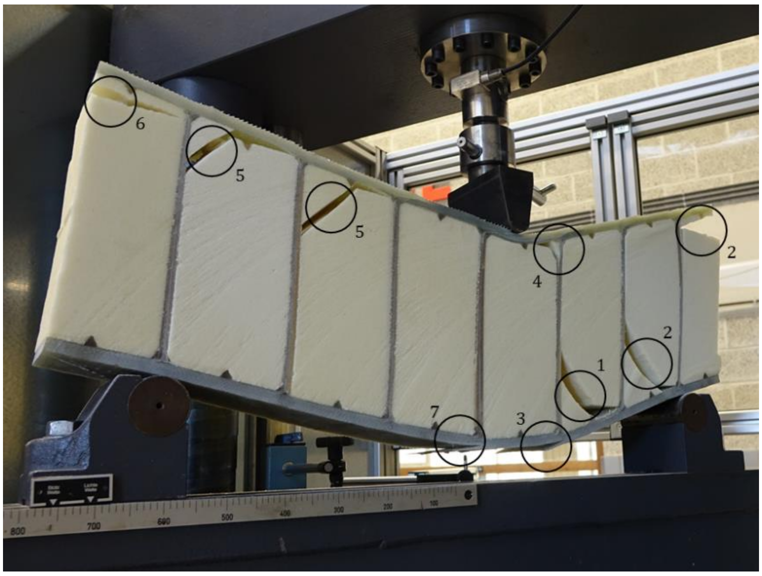


**Figure 5.** Asymmetrically loaded unit cell specimen with foam at ultimate failure during the 3PB test with an indication of the local failure events.

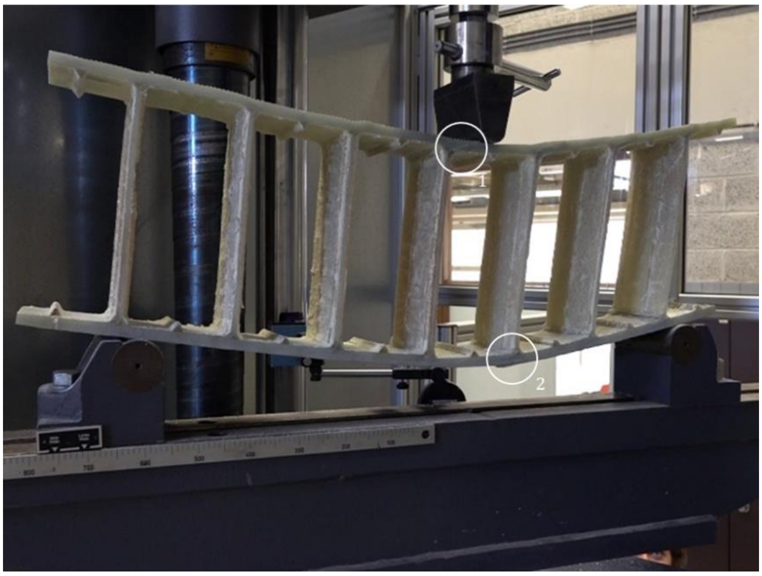


**Figure 6.** Asymmetrically loaded unit cell specimen without foam at ultimate failure during the 3PB test with an indication of the local failure events.

The measured vertical deflection at 1kN (See Figure 5) is 4.85 mm. This value can be analytically or numerically predicted using properties based on engineering constants determined by CLT ($E_{x,flange}$ = 23,069 MPa; $E_{x,web}$ = 10,153 MPa) and the average measured thicknesses of the flanges (11 mm) and webs (7 mm). Using these values, the predicted deflection at 1 kN is equal to 3.50 mm. The difference between the measured and predicted deflection can be attributed to the reduction in the CLT predictions caused by the tiling, as well as to the localized compression of the flanges at the point of load introduction and supports.

**Table 1.** Deflection and force values and description of the failure mechanism of the different local failure events during the 3PB test of the unit cell with foam.

| No. | Deflection [mm] | Force [kN] | Failure Mechanism |
|---|---|---|---|
| 1 | 17.07 | 10.55 | Crack initiation at the bottom of the foam in field 6 |
| 2 | 21.21 | 10.32 | Crack initiation at the bottom of the foam in fields 7 and 8 |
| 3 | 29.25 | 9.06 | Delamination of the bottom flange in field 5 |
| 4 | 33.60 | 8.64 | Crack initiation at the top of the foam in field 5 |
| 5 | 55.43 | 10.28 | Crack initiation at the top of the foam in fields 2 and 3 |
| 6 | 71.96 | 9.52 | Crack initiation at the top of the foam in field 1 |
| 7 | 75.94 | 8.02 | Delamination of the bottom flange in field 4 |

**Table 2.** Deflection and force values and description of the failure mechanism of the different local failure events during the 3PB test of the unit cell without foam.

| No. | Deflection [mm] | Force [kN] | Failure Mechanism |
|---|---|---|---|
| 1 | 41.05 | 4.75 | Delamination in the top flange in field 5 |
| 2 | 66.89 | 4.07 | Delamination in the bottom flange in field 5 |

## 3. Fatigue Test Specimen and Setup

Despite the foam blocks positively impacting the web buckling stability and substantially reducing the deflections, they are not considered in GFRP foot and road bridge design due to their degradation over the bridge's 100-year lifespan [10,26,27], rendering them structurally insignificant. Consequently, the PUR foam cores are carefully removed before conducting fatigue tests on the unit cell specimens, enabling the observation of crack initiation and propagation within the specimens. While this removal prevents the study of flange/foam core debonding, it investigates delamination branching into the flanges through inclined crack propagation between tiled plies in the transverse bridge span direction during fatigue tests. An extreme impact on the bridge deck top flange is simulated by manually initiating a crack at the most adverse location, at the connection between the top flange and the web between the fourth and fifth fields (left of the loading nose) of the unit cell, based on findings from Figure 6.

Figure 7 illustrates a close-up of the first failure and crack paths (indicated by the white arrows) for the asymmetric static 3PB test on a unit cell specimen without foam cores and without crack initiation of Section 2. The starting point of the crack initiation in Figure 7 is given by the circle marker, while the arrest location of the crack in the test is illustrated by the cross. The crack in the top flange is stopped by the 90° ply (black dotted line) wrapped around the foam cores. As a result, a crack between the internal foam cores and the top flange, creating two separate parts (i.e., total failure of the element), is unlikely. In the experimental fatigue tests, an extreme situation is examined in which an accidental event (i.e., for example, a heavy object falling on the bridge deck) causes a crack in this 90° ply. For this, crack initiation (i.e., red fine dotted line) in the unit cell specimens is applied over the full depth on the inside of the fourth field of the unit cell using a Dremel tool with a diamond blade. Only the 90° ply is cut through, directly connecting the inside of the web-core sandwich and the top flange via the resin-rich zone in the connection.

Experimental input on the fatigue life of the damaged unit cell is obtained through 2D 3PB asymmetric fatigue tests at various load levels using a servohydraulic Instron 8801 fatigue testing system [28] equipped with a 100 kN load cell as depicted in Figure 8. The unit cell specimen without foam cores and with crack initiation is supported by two steel rollers rigidly connected to the support system. These supports are mounted on an I-profile to achieve the correct span length and connected to the hydraulic actuator using a solid steel connector block and an M30x2 connector. Displacement is applied through the lower structure, with a cylindrical loading nose connected to the load cell and the machine's crosshead via a threaded screw (M30x2). The equipped load cell on the fatigue testing system has an accuracy of ±0.002% of the load cell capacity or 0.5% of the indicated load, whichever is larger. Furthermore, the hydraulic actuator at the bottom of the testing machine is also equipped with an anti-rotation device to prevent possible rotations around the longitudinal axis of the actuator during the execution of the fatigue test. For this purpose, an H-frame is fitted around the actuator with two bearings at the ends, rolling on a rigid steel bar.

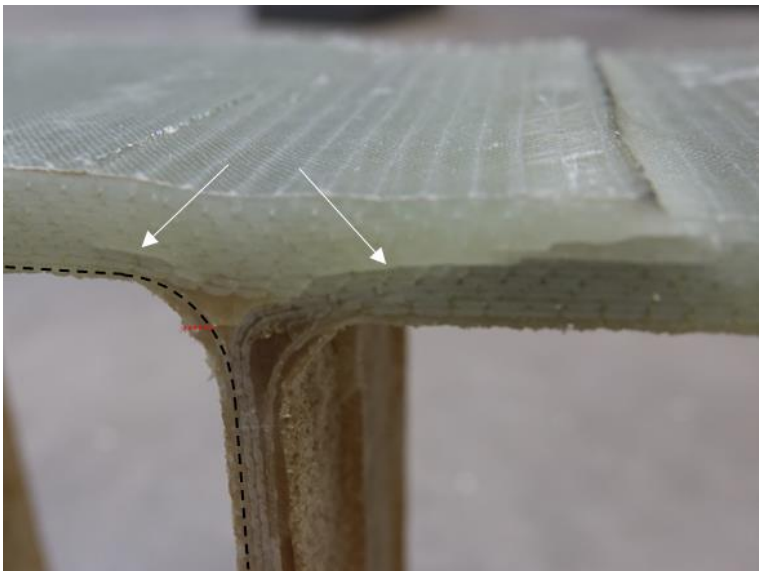

**Figure 7.** Crack path (indicated by white arrows) after static 3PB test from Section 2 and manually applied crack initiation (red line) through the 90° ply (black dotted line) around the foam core.

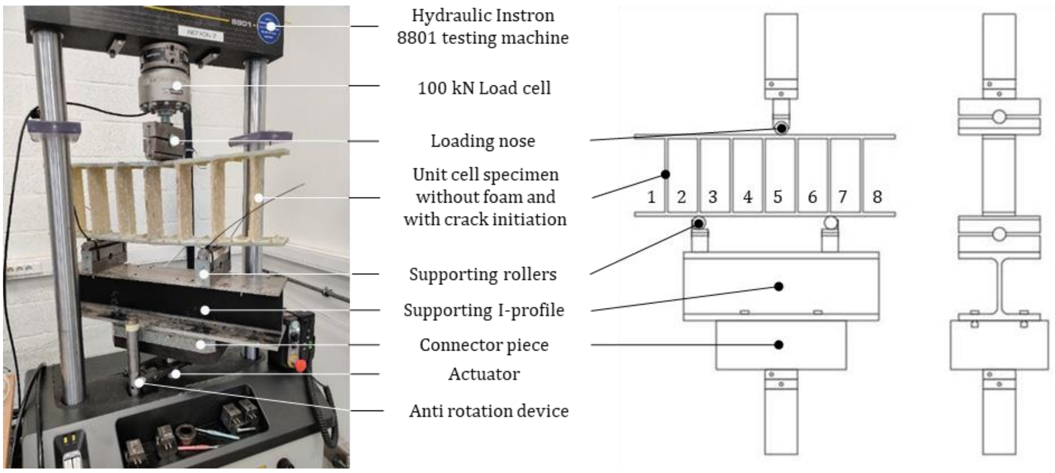


**Figure 8.** A 3PB asymmetric fatigue test setup on servohydraulic Instron 8801.

All tests are instrumented using DIC for full-field strain mapping and online microscopy to monitor crack position and progression. DIC involves applying a speckle pattern at the flange–web connection to monitor local deformations, while online microscopy utilizes a white base coat applied only to the investigated region, aiding crack propagation monitoring. These techniques are applied separately to the top and bottom flanges, focusing on regions around the connection of the top and bottom flanges with the fourth web (between the fourth and fifth unit cell) as depicted in Figure 9. First, DIC is performed on the top and bottom flanges to track the strains in both intersections. Secondly, online microscopic imaging is executed on the top and bottom flanges. The two techniques are never combined on one specimen to allow for good lighting and exposure of both camera setups.

(**a**) (**b**)

**Figure 9.** (**a**) Close-up of the top flange–web intersection with crack initiation and a white base coat for online microscopy; (**b**) close-up of the bottom flange–web intersection with a DIC speckle pattern (right), a reverse combination is also possible.

## 4. Determination of Fatigue Setup, Loading Procedure, and Fatigue Load Values

The basic fatigue loads are established at 50%, 60%, and 80% of the load leading to the first observable failure, as detailed in Section 2. These values are selected as an initial approximation for assessing the failure characteristics of the TS unit cells in high-cycle fatigue tests, as there are presently no standards or guidelines offering reasonable indications. According to Figure 6 and Table 2, the initial failure load for a unit cell without foam cores, with a 600 mm span, is 4.75 kN, resulting in a maximum fatigue load of $F_{fat}$ = 4.75 kN 60% = 2.85 kN. However, during the initial fatigue test with a 600 mm span, the lateral out-of-plane displacements of the cross-section were too severe, potentially jeopardizing the testing equipment. Additionally, achieving the desired fatigue load required a significant stroke, limiting the load frequency and introducing accuracy issues with the imposed load. Consequently, it was decided to reduce the span length for the fatigue tests.

To investigate the impact of span length on deflection and internal strain/stress distribution, an FEA model was introduced with an inserted crack in the web at the intersection to simulate crack initiation in experiments. A unit load of 1 kN was applied in the numerical model, and the results were validated against experimental results from a new static 3PB test on a unit cell specimen without foam blocks but with crack inclusion. The numerical model with a 600 mm span yielded a deflection of 5.05 mm, closely matching the experimental deflection of 5.07 mm. Figure 10 illustrates the numerically determined deflection with varying span lengths, where a 0 mm support length corresponds to a fully supported bottom flange.

Moreover, internal strains at the intersection of the top flange and the web were compared between the numerical model and the experimentally obtained results for a 3PB test with a 600 mm support length and a unit load of 1 kN. DIC images of the top flange were processed for the experimental data, with two paths (consisting of 200 points) applied—one at the top (L1) and one at the bottom (L0) of the flange—as depicted in Figure 11.

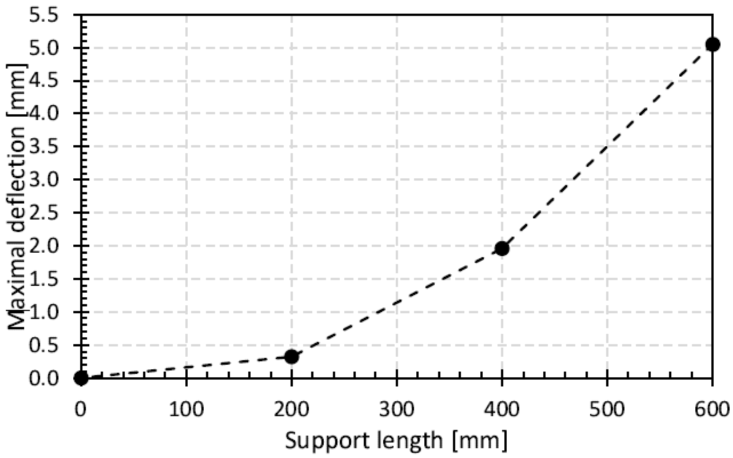


**Figure 10.** Numerical deflection evolutions as function of the span length.

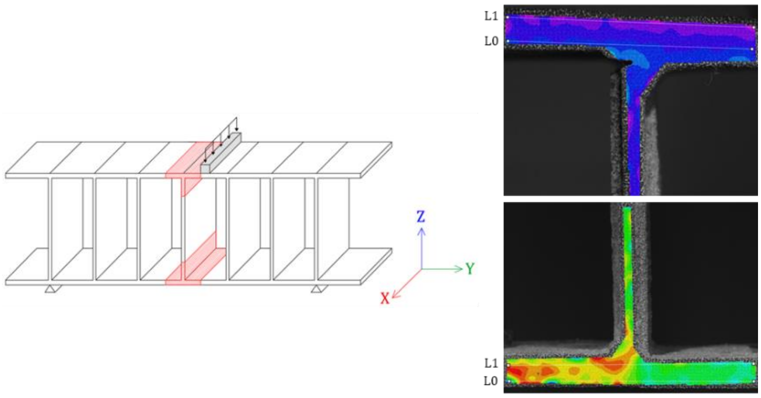


**Figure 11.** DIC images of the top and bottom flanges with the position of the L0 and L1 paths.

Two similar paths in terms of length and location were then applied to the numerical model. The relative distance between the paths in the VIC-3D 8 software is approximately 6 to 7 mm; however, the thickness of the top and bottom flanges is not uniform along the length of the path, and as a result, the path is more towards the centre of the flange in some locations. This can be seen in Figure 11 (left) where the L0 path to the right of the web is closer to the centre of the flange compared to the L0 path to the left of the web. This has an influence on the magnitude of the strain values from the DIC analysis. However, this phenomenon does not occur in the numerical FEA model, which may lead to possible deviations between the two.

The numerical and experimental strain results under a unit load of 1 kN for the path at the top and bottom of the top flange are shown in Figure 12. It should be noted that the positioning of the paths in the thickness direction of the flanges has an important influence on the magnitude of the obtained strain values due to the stress development in the thickness direction and the limited thickness of the top flange. It is impossible to guarantee an exact match in the positioning of the paths in the numerical model and in the DIC processing software, which means that deviations are possible in the data below.

Figure 12 illustrates that there is reasonable agreement between the experimental and numerical strain values, both falling within the same strain range. Numerical values tend to be slightly higher, ensuring a more conservative approach. In conclusion, the numerical FEA model provides a reasonable representation of actual strain values in the unit cell specimen.

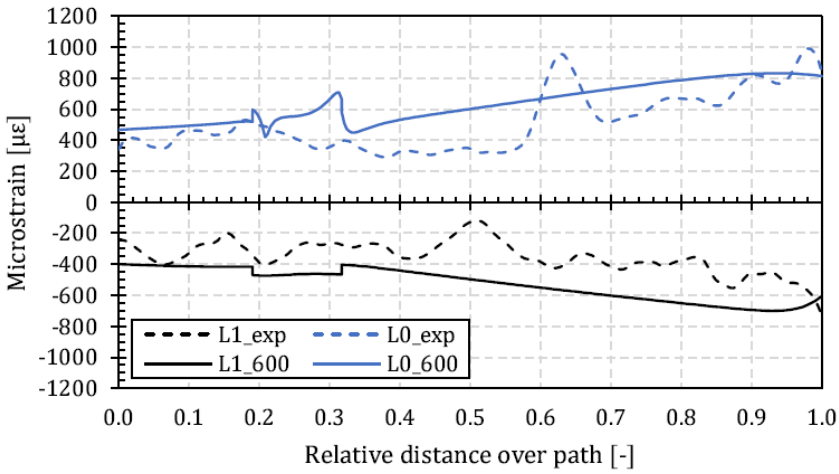


**Figure 12.** Experimental DIC and numerical FEA strain profile over the path at the top (blue) and bottom (black) of the top flange with a span of 600 mm under a unit load of 1 kN.

To attain a similar stress development in the flanges and webs of the unit cell specimen in experimental fatigue tests with reduced span compared to static load tests with a 600 mm span, the fatigue load must be increased. The amplification degree is determined based on the strain value ratios from the numerical model. Figure 13 depicts strains over paths at the top and bottom of the top flange at the web intersection between fields four and five for a span length change, with supports always placed directly under the webs.

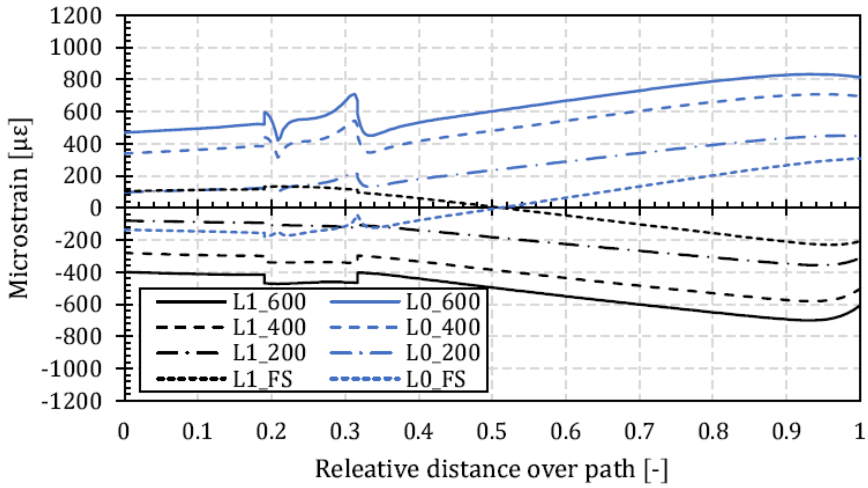


**Figure 13.** Numerical FEA strain profile over the path at the top (blue) and bottom (black) of the top flange for different span lengths under a unit load of 1 kN.

Based on Figure 10, the span length was reduced to 400 mm for the fatigue tests, resulting in more than a 50% reduction in deflection at a unit load of 1 kN. Furthermore, Figure 13 suggests that, with a 400 mm span, the strain profile closely resembles that of the static load test on the unit cell specimen. A more severe span reduction noticeably alters the strain profile in the top flange. Assuming linear elastic behaviour, to achieve similar strain values, the force must be increased by a factor of 1.30. Consequently, the maximum fatigue load becomes $F_{fat}$ = 4.75 kN·60%·1.30 = 3.71 kN. For simplicity of testing, this fatigue load is rounded to the nearest integer, resulting in $F_{fat}$ = 4.00 kN, equivalent to 65% of the first failure load during the static 3PB test. The applied fatigue load generates maximum strains of −2901 µs and 3537 µs (i.e., −35 MPa and 43 MPa) at the top and bottom of the top flange, respectively. In the connection of the fourth web with the top and bottom flange, the strains reach −1719 µs and 2715 µs (i.e., −17 MPa and 28 MPa), respectively.

To prevent movement of the test specimens during the downward stroke of the actuator, a minimum load equivalent to 10% of the maximum fatigue load is maintained on the specimen. Based on the maximum and minimum fatigue load values, the average fatigue load can be calculated, indicating the load magnitude. The minimum and average loads are 0.4 kN and 2.2 kN, respectively. The fatigue test is conducted in a force-controlled manner, with the actuator's deflection indicating specimen degradation with increasing cycle count.

Given the certain relaxation of the unit cell specimens, even without foam, a limited load frequency of 2 Hz is adopted. As a result, the load is sufficiently slowly introduced so that it may be transferred over the entire specimen to the supports. The load introduction at the start-up of the fatigue test is shown in Figure 14. The specimen is first statically preloaded to the average load value of 2.2 kN (1), after which the load is gradually increased until the maximum and minimum fatigue load is reached (2). The desired amplitude of the fatigue cycle is reached after about 300 to 400 cycles or 150 to 200 s.

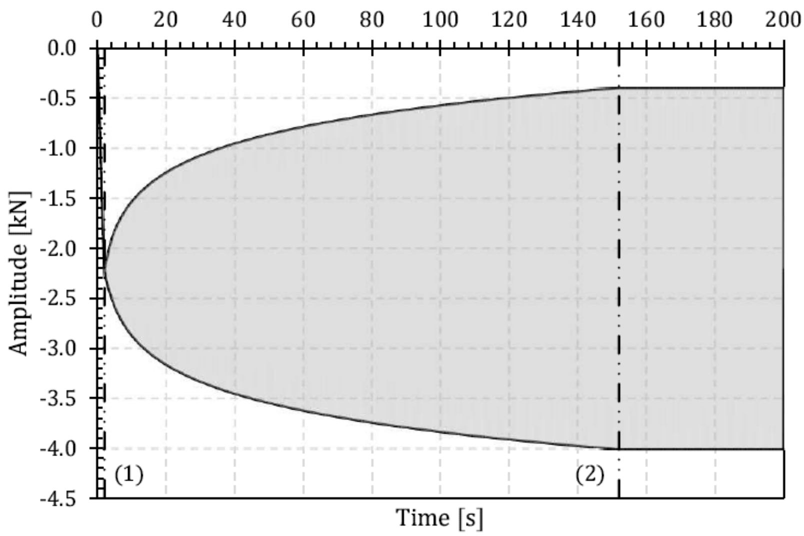


**Figure 14.** Amplitude evolution during preloading (1), start-up (2), and execution of the fatigue test with a maximum and minimum fatigue load of 4.0 kN and 0.4 kN, respectively.

Before commencing the fatigue test, a reference static linear-elastic deformation test is performed up to a load of 2 kN, instrumented with DIC. Subsequently, at regular intervals during the fatigue test, additional static 3PB tests are conducted with a maximum load of 2 kN, utilizing DIC to monitor stiffness modifications and crack propagation in the unit cell specimens. The intervals of the static tests (i.e., the number of cycles imposed) depend on the time of day, as measurements can only be executed during the day due to manual execution, while this is not possible overnight. The fatigue tests are stopped until the ultimate failure of the specimens, triggered automatically by the imposed deflection limits in the testing machine.

Following this, different load levels involving crack initiation at the top flange are studied. Maximum fatigue loads of 3.0 kN and 5.0 kN are used, corresponding to approximately 50% and 80% of the first failure load, respectively. Additionally, the influence of damage initiation at the bottom flange is examined.

## 5. Fatigue Test Results

The results of the deflection (i.e., relative displacement of the actuator) as a function of the logarithmic total number of imposed cycles are shown in Figure 15. Here, the different types of fatigue tests in terms of loading and crack location are represented by separate line types. Furthermore, an abbreviation consisting of three parts is used, namely, first, a number indicating the maximum fatigue load, followed by the location of the crack initiation, and finally, the test specimen number separated by a dash.

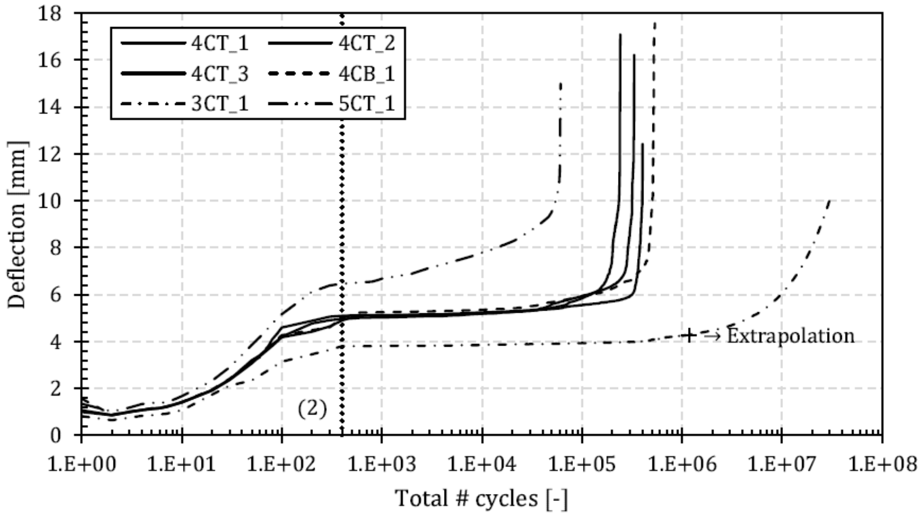


**Figure 15.** Deflection as a function of the logarithmic total number of imposed cycles for the different fatigue test specimens.

Figure 15 provides insights into the unit cell test progression. Initially, the start-up phase of the test is evident, marked by a significant increase in deflection within the first 100 cycles, followed by a stabilization around the 400-cycle mark. Subsequently, a prolonged plateau phase ensues, characteristic of composite materials and structures. The third and final phase sees rapid degradation, driven by the force-based testing method, culminating in the ultimate failure of the unit cell specimen.

For unit cell test specimens subjected to a fatigue load of 4 kN with crack initiation at the top flange (4CT), the maximum total number of cycles falls within the range of 241,000 to 402,000 cycles, with an average value of 325,000 cycles. When the same fatigue load magnitude is applied with crack initiation at the bottom flange (4CB), the number of cycles to ultimate failure increases to 534,000 cycles. This indicates that a crack at the intersection between the top flange and a web has a more detrimental effect on the element's robustness compared to damage at the bottom flange.

Subsequently, with an increased fatigue load of 5 kN (5CT), the number of cycles sharply decreases by 80% to a maximum of 61,000 cycles. Conversely, with a reduced fatigue load of 3 kN (3CT), the number of cycles increases significantly to more than 30,000,000 cycles. However, this value represents an extrapolation for the plateau phase in this fatigue test, as the fatigue test with a load of 3 kN was stopped at 1,173,000 cycles due to time constraints. The maximum number of cycles at ultimate failure was determined based on linear extrapolation to a deflection corresponding to failure onset in the other specimens. It is worth noting that while failure onset in the other fatigue tests occurred at a deflection of approximately 10 mm, the specimens still retained some residual strength beyond this limit, requiring additional cycles until ultimate failure. However, these were not included in the linear extrapolation due to potential errors in estimation.

Figure 16 presents the total number of cycles to failure for the unit cell test specimens under different fatigue loads. The secondary axis on the right displays the relationship between the fatigue load and the maximal σ22 stresses just before the connection between the fourth web and the top flange (the location of crack initiation) according to the FEA model of the unit cell. A linear relationship between the measured values is established, represented by a linear trendline. To account for potential inaccuracies, deviations, and scatter in the test results, the trendline is reduced by one standard deviation. The absolute value of the slope of the trendline through the measurement points is determined to be 0.28.

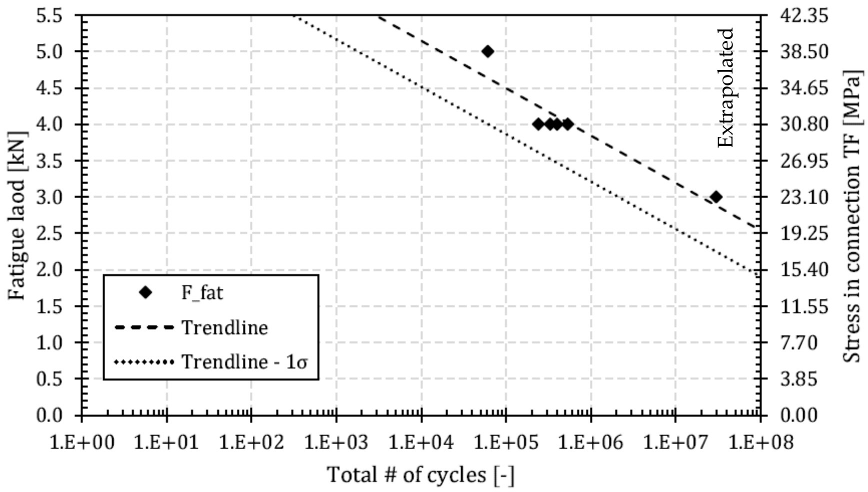


**Figure 16.** The linear trend line for the fatigue load in the function of the logarithmic total number of imposed cycles to ultimate failure.

Apart from determining the maximum number of cycles leading to failure, an examination of the stiffness degradation of the unit cell test specimen throughout the fatigue test is conducted based on the force–deflection data obtained from the testing machine and DIC. The stiffness analysis was specifically conducted for the three specimens designated as 4CT. In Figure 17, the absolute force values are plotted against deflection (i.e., the relative position of the actuator) for various intermediate measurements of the 4CT_1 specimen. To simplify the figure, only the loading phase of the static 3PB test data are included. Additionally, the figure provides labels indicating the number of completed cycles in the fatigue test along with the associated data. The static 3PB test commences at a load of 0.4 kN, which is the minimum load required to secure the test specimen in place during the fatigue test.

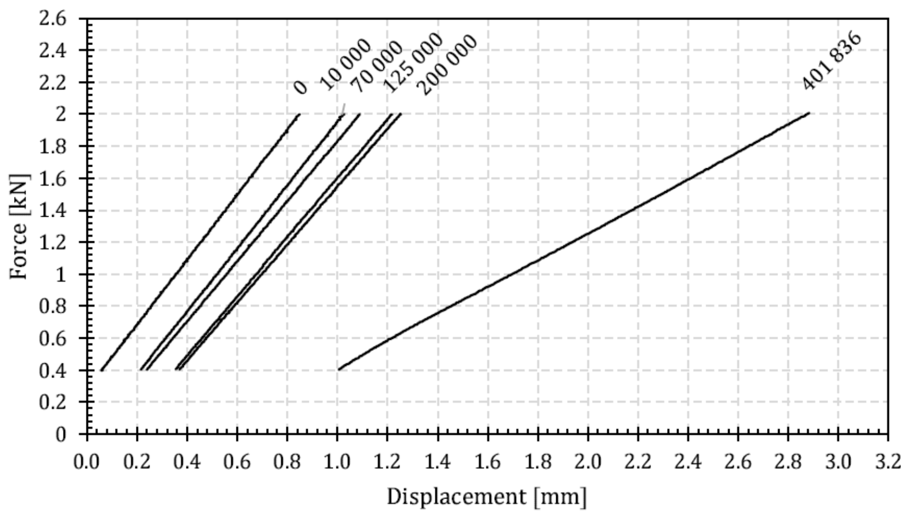


**Figure 17.** Bending stiffness degradation from the static 3PB tests at different numbers of cycles in the force–displacement graph from 4CT_1.

Figure 17 illustrates a progressive increase in deflection required to maintain the minimum load of 0.4 kN as the number of cycles advances. Following an initial phase with a slight increase, the deflection remains relatively stable before undergoing a substantial increase leading up to the ultimate failure of the specimen, which aligns with the observations made in Figure 15. Similarly, the stiffness, represented by the slope of the force–deflection curve, exhibits a slight initial decrease, followed by a pronounced decline until reaching ultimate failure.

The flexural stiffness relative to the initial value at 0 cycles calculated based on the intermediate bending tests of the three specimens is depicted in Figure 18, as a function of the total number of cycles. Notably, the stiffness experiences a relatively modest reduction of approximately 12% up to 200,000 cycles, after which it undergoes a substantial decrease. This finding corroborates the trends observed in Figure 15.

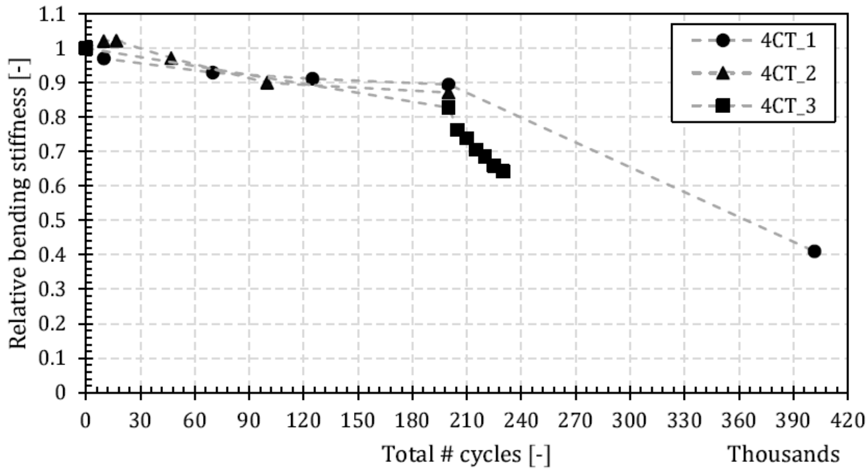


**Figure 18.** Relative bending stiffness for a fatigue load of 4.0 kN (approx. 65% of the first failure load), as a function of the total imposed 401,836 cycles.

### 5.1. DIC Analysis of the Flange/Web Connection

In addition to assessing the overall impact of the fatigue load on the service life of the unit cell specimens, the localized effects at critical locations within the unit cell cross-section are also investigated, based on DIC images. Both the reference static 3PB test and the numerical FEA model indicate that laminate failure and the highest stress levels occur at the intersection between the web, situated just to the left of the loading nose, and the top and bottom flanges. At these distinct locations, given the availability of only one DIC camera setup for each, DIC analyses are conducted to monitor strain evolution. The fatigue test is briefly paused at regular intervals to perform a static 3PB test concurrently with DIC image capture. The displacement-controlled 3PB test is executed at a load rate of 2 mm/min, reaching a load of 2 kN, after which the unit cell specimens are unloaded at an equivalent speed to reach the minimum fatigue load.

Figures 19–21 depict the Lagrange εxx, εyy, and εxy evolution at the intersection of the web and the top flange under a 2 kN load throughout the fatigue test. DIC images from specimen 4CT_1 are presented at six different intervals: 0 (reference); 10,000; 40,000; 100,000; 200,000; and 300,000 cycles. For clarity, uniform colour scale limits are employed within each figure to visualize the strain evolution across the various images.

Primarily, Figure 19 reveals the expected compression at the top and tension at the bottom of the top flange. Additionally, both Figures 19 and 20 suggest the development of tension in the x- and y-directions above the crack and compression just before the crack's tip, with these effects intensifying as the fatigue test progresses. This strain distribution contributes to crack growth in two directions: interlaminar toward the loading nose and in the y-direction. Moreover, Figure 21 indicates the presence of shear strains at both locations.

Figures 22–24 depict the Lagrange εxx, εyy, and εxy evolution at the intersection of the web and the bottom flange at a load of 2 kN during the fatigue test. The DIC images are from specimen 4CT_2 at 0 (i.e., reference), 10,000, 17,000, 470,000, 100,000, and 200,000 cycles. In the figures, constant limits for the colour scale are used to display the strain evolution between the different images of a figure.

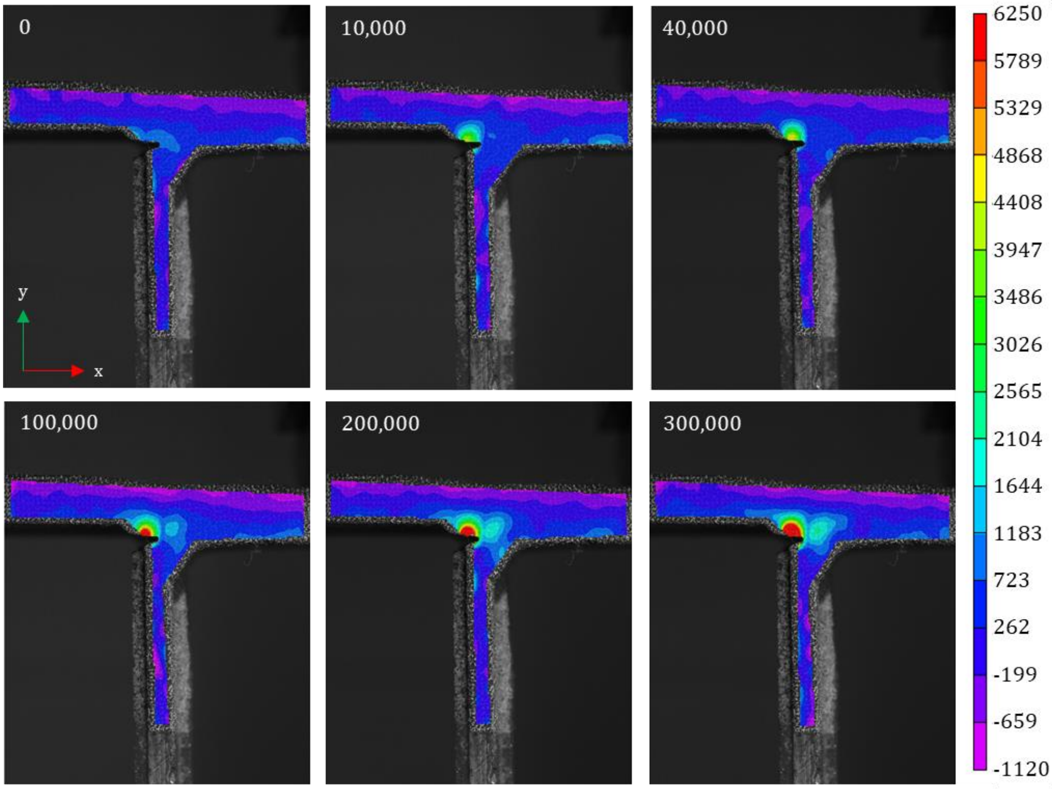


**Figure 19.** Lagrange strain in the x-direction (εxx) at the intersection of the top flange and web for a load of 2 kN at different numbers of cycles from specimen 4CT_1.

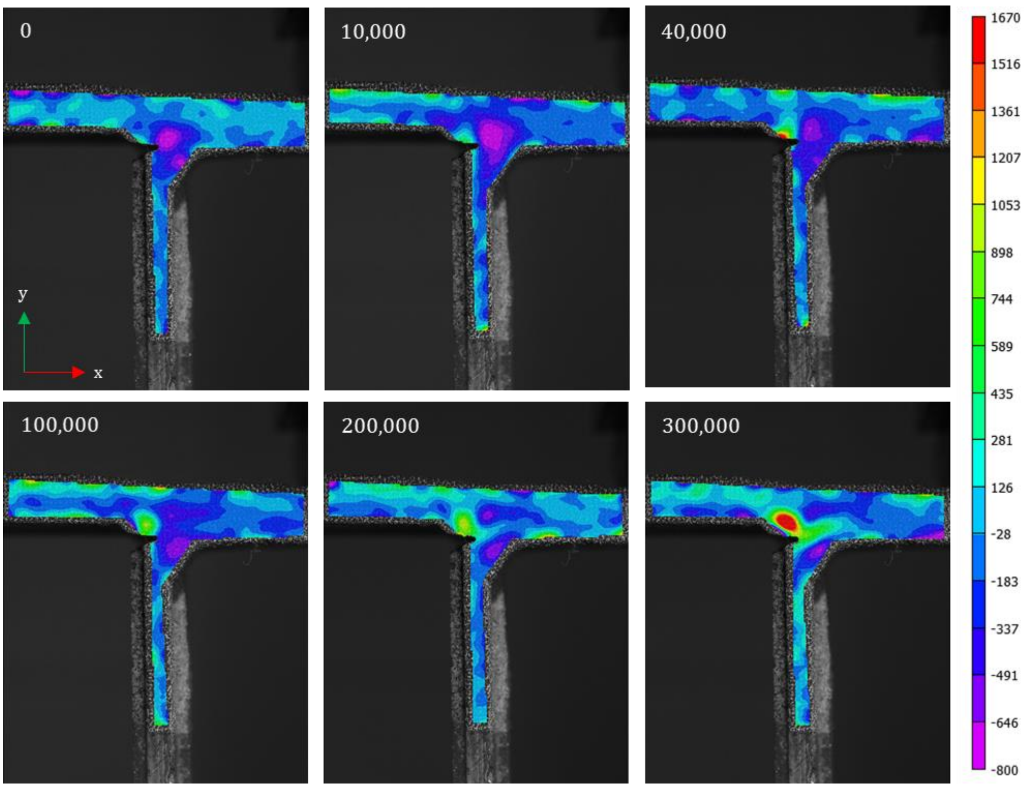


**Figure 20.** Lagrange strain in the y-direction (εyy) at the intersection of the top flange and web for a load of 2 kN at different numbers of cycles from specimen 4CT_1.

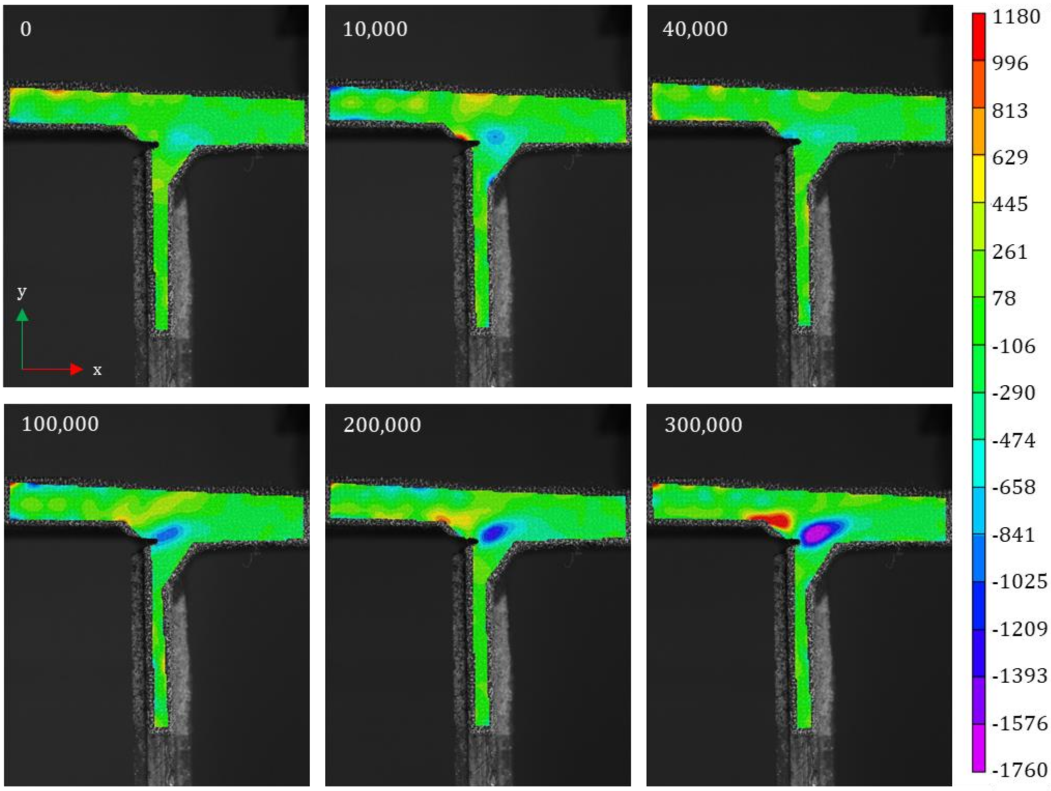


**Figure 21.** Lagrange shear strain in the xy-plane (εxy) at the intersection of the top flange and web for a load of 2 kN at different numbers of cycles from specimen 4CT_1.

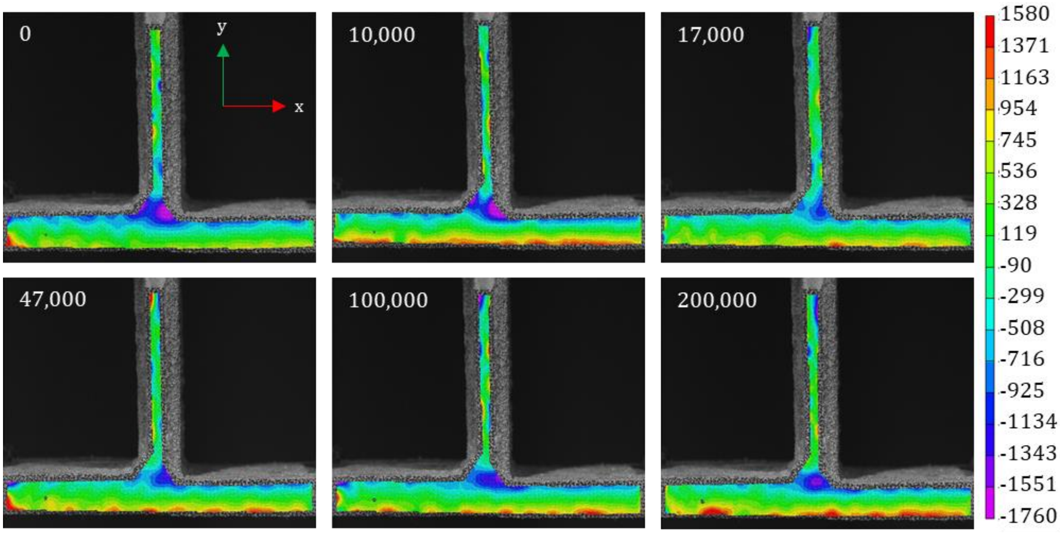


**Figure 22.** Lagrange strain in the x-direction (εxx) at the intersection of the bottom flange and web for a load of 2 kN at different numbers of cycles from specimen 4CT_2.

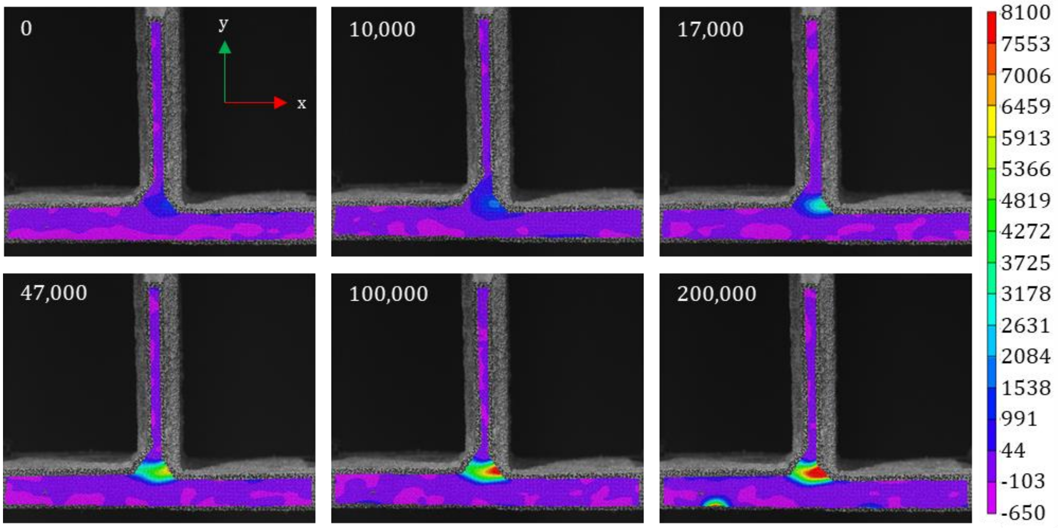


**Figure 23.** Lagrange strain in the y-direction (εyy) at the intersection of the bottom flange and web for a load of 2 kN at different numbers of cycles from specimen 4CT_2.

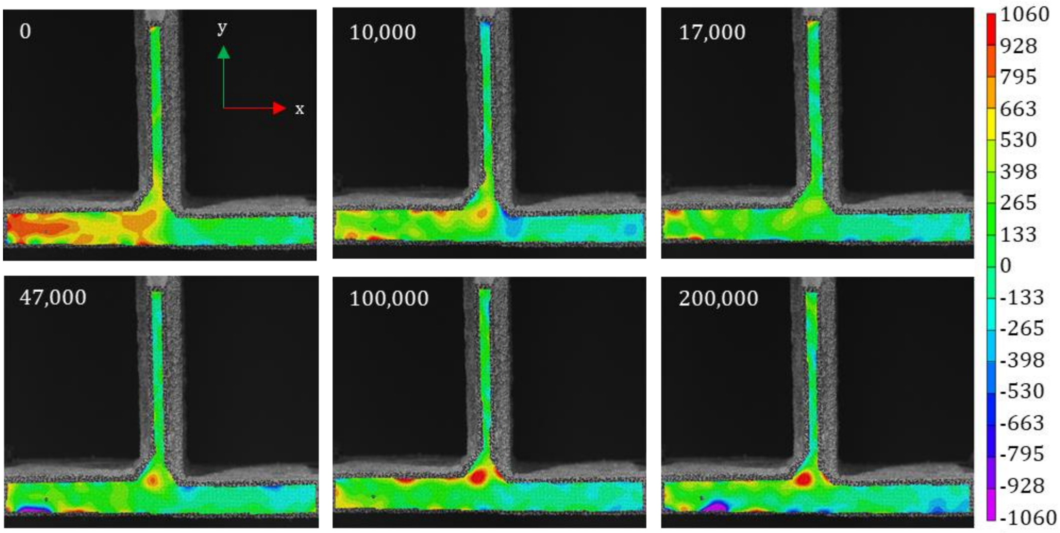


**Figure 24.** Lagrange shear strain in the xy-plane (εxy) at the intersection of the bottom flange and web for a load of 2 kN at different numbers of cycles from specimen 4CT_2.

Figures 22 and 23 illustrate the accumulation of tensile and compressive strains at the connection of the web and the bottom flange along the side of the fifth load field. This strain build-up coincides with the formation of an interlaminar crack. Towards the end of the fatigue test (i.e., at 200,000 cycles), a concentration of tensile strain becomes apparent on the lower left side of the lower flange, precisely at the location of a free-ply edge. Additionally, Figure 24 reveals the presence of shear strain build-up at this location.

### 5.2. Fatigue Behaviour Analysis

The typical failure behaviour of the unit cell specimens during the fatigue test is presented in Figure 25 for specimen 4CT_3, along with two close-up views of the failure locations at the top and bottom flanges. It is observed that, during the fatigue test, initial failure consistently originates in the bottom flange, followed by the development of a crack in the top flange. At both failure locations, interlaminar failure occurs due to compressive and tensile stresses in the top and bottom flanges, respectively. The formation of cracks in the top and bottom flanges occurs relatively early in the testing process. However, these small cracks remain stable, allowing the unit cell specimens to endure a substantial number of cycles under a 4 kN fatigue load. Only in the final phase of testing do the cracks progressively grow under shear stresses until reaching the ultimate failure of the unit cell specimen. The fatigue test was halted for safety reasons upon reaching a displacement limit. At this point, the bending stiffness of the unit cell specimen had significantly decreased, which would have resulted in substantial deflection and rendered the bridge deck unusable.

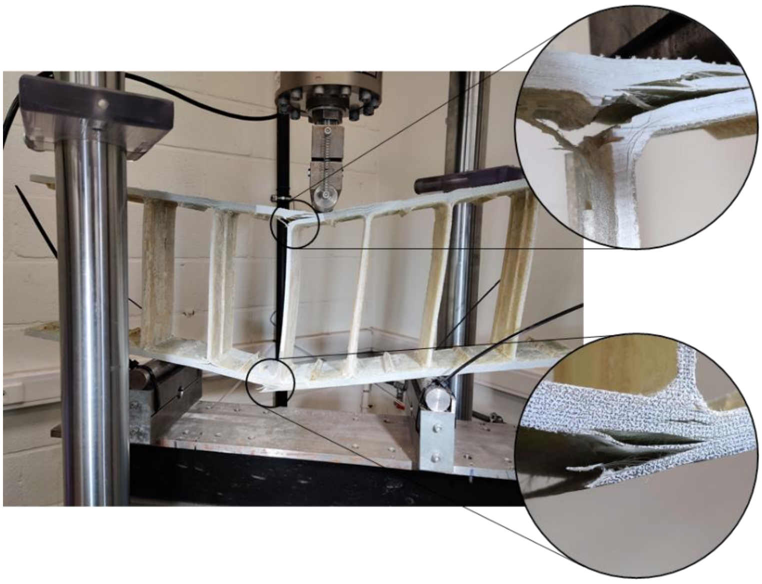

**Figure 25.** The ultimate failure of specimen 4CT_3 with a close-up crack image at the top and bottom flanges.

Figures 26 and 27 provide detailed views of the initiation and progression of cracks at the intersection of the web with the top and bottom flanges during the fatigue test for specimens 5CT_1 and 4CB_1, respectively. These images were captured using a DinoLite online microscope at intervals of 30 min. The areas of interest are coated with a white basecoat to enhance contrast and improve the detection of very fine crazing cracks at the intersections of the unit cell specimen. Figures 26 and 27 illustrate key moments in the crack initiation and progression until reaching ultimate failure (i.e., the last image).

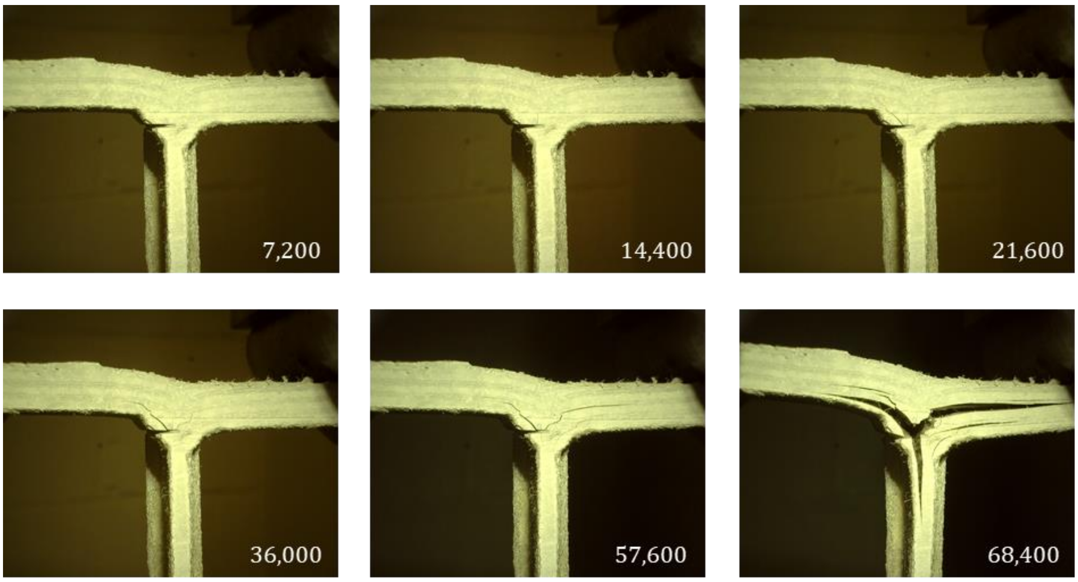


**Figure 26.** Online microscopic imaging of the crack initiation and progression in the top flange and web for specimen 5CT_1 at different numbers of cycles.

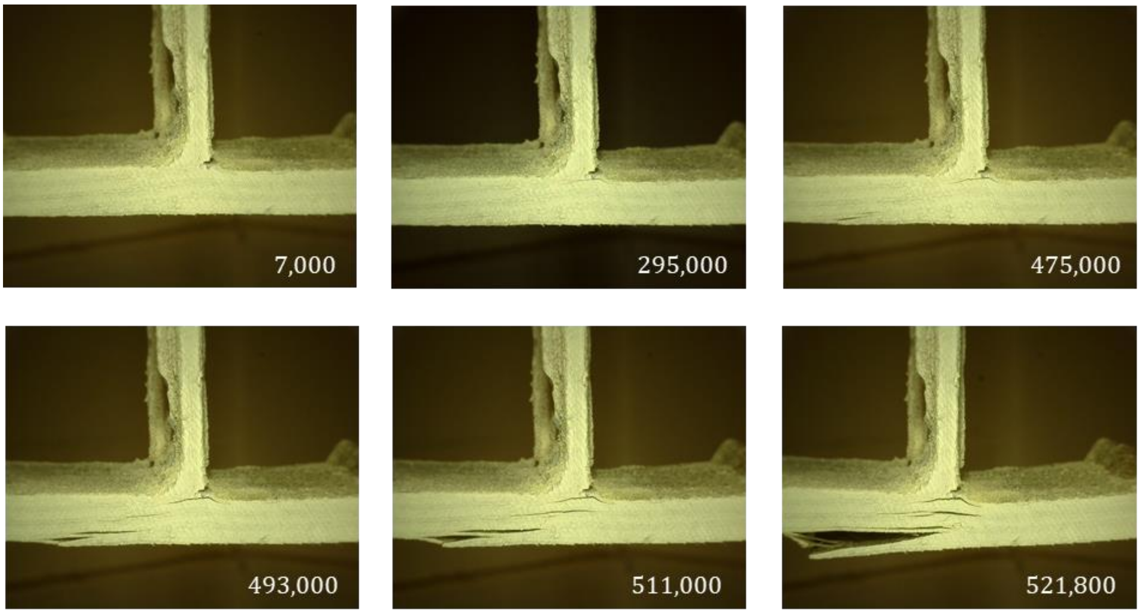


**Figure 27.** Online microscopic imaging of the crack initiation and progression in the bottom flange and web for specimen 5CT_1 at different numbers of cycles.

The initiation and progression of cracks in the top and bottom flanges exhibit similar patterns, as revealed by the DIC strain evolution shown in Figures 19–24. In Figure 26, interlaminar crazing cracks initially appear in the top flange between the 90° ply around the foam core, occurring approximately after 21,600 cycles. Subsequently, crazing cracks develop in the direction of the applied crack initiation location, starting around 36,000 cycles. Both crazing cracks continue to expand and open further as the fatigue test advances, accompanied by the formation of secondary interlaminar cracks in adjacent plies due to shear stresses. However, a direct connection from the applied crack initiation to the top of the top flange through the various plies is not established in any scenario. Nevertheless, the bending stiffness of the top flange experiences a significant reduction due to the failure of the interlaminar connection between the individual plies. In the event of ultimate failure of the unit cell specimen, interlaminar crack growth also occurs between the 90° ply and the $\pm45°$ plies of the webs near the bottom flange.

In the lower flange, as depicted in Figure 27, interlaminar crazing cracks initially form between the 90° ply and the plies of the lower flange, occurring approximately after 295,000 cycles, at the location of the intersection on the right side of the web. However, this crack remains relatively stable throughout the remainder of the fatigue test, with minimal growth in the transverse direction of the bottom flange. Conversely, the crack that develops on the underside of the bottom flange, at the location of a free-ply edge, progressively increases in size and length during the fatigue test. Additionally, starting from this location, interlaminar cracks develop between the overlying plies, advancing towards the initially formed crack to the right of the web. Similarly to the top flange, there is no connection in the thickness direction through a ply between the different interlaminar cracks, and only the interlaminar connection between the individual plies in the bottom flange is disrupted. Consequently, the bending stiffness decreases significantly at this location, leading to the failure of the unit cell specimen.

The failure mechanism remains consistent among the different specimens in the fatigue test, with variations in the rate of crack growth and, consequently, specimen degradation depending on the applied fatigue load magnitude.

## 6. Conclusions

This study investigated the fatigue performance and crack evolution of tiled sandwich unit cell panels through controlled fatigue testing, with induced crack initiation sites located between the web and top flange under varied load conditions. The findings offer valuable insights into the structural response and damage tolerance of these unit cell panels, which have potential applications in high-demand engineering environments.

The fatigue behaviour observed in these panels follows a three-phase pattern characteristic of conventional composite materials:

1. Initial Stiffness Degradation: During the early cycles (approximately 400–500), rapid stiffness reduction occurs, alongside the appearance of transverse crazing cracks. These initial cracks are critical indicators of the panel's response under cyclic loading, marking the transition to the next phase.
2. Plateau Phase: Following initial degradation, a stable phase is observed, where stiffness degradation stabilizes, and existing cracks remain unchanged. The duration of this phase is highly dependent on the magnitude of applied loads, suggesting that moderate loading may preserve structural integrity over more cycles.
3. Final Degradation and Failure: The third phase is marked by accelerated stiffness loss and significant crack propagation across the specimen's cross-section, eventually resulting in failure. This phase occurs within a few thousand cycles, highlighting the influence of load intensity on fatigue life.

The use of DIC (digital image correlation) allowed for precise strain mapping, identifying key points of strain concentration that drive crack initiation and growth:

- At the manually induced crack tip;
- At the web-to-bottom flange connection;
- Along the free-ply edge of the bottom flange.

These strain concentrations facilitate the formation of initial cracks at the bottom flange's ply edge, followed by crack development from the induced initiation point. Notably, crack propagation is largely interlaminar, progressing within the bottom flange towards the web and extending toward the applied load in the top flange. Importantly, cracks remain confined within the internal structure, avoiding direct exposure to the external environment, which underscores the damage-tolerant design of these panels.

Implications for Engineering Applications: The observed fatigue resistance and damage tolerance of tiled sandwich panels position them as promising candidates for structural applications requiring durability, such as bridge construction and other critical load-bearing installations. The interlaminar crack propagation without through-thickness penetration indicates a self-contained failure mode that enhances structural resilience. These findings not only deepen our understanding of tiled sandwich composites' behaviour under cyclic loading, but also contribute to design strategies for robust and resilient composite structures in various engineering domains.

**Author Contributions:** Conceptualization, W.D.C. and W.V.P.; methodology, J.U.; software, J.U.; validation, J.U., W.D.C. and W.V.P.; formal analysis, J.U.; investigation, J.U.; resources, W.D.C. and W.V.P.; data curation, J.U.; writing—original draft preparation, J.U.; writing—review and editing, W.D.C. and W.V.P.; visualization, J.U.; supervision, W.D.C. and W.V.P.; project administration, W.D.C. and W.V.P.; funding acquisition, J.U. All authors have read and agreed to the published version of the manuscript.

**Funding:** This research was funded by FWO-Flanders, grant number 1S50522N.

**Data Availability Statement:** The data presented in this study are available on request from the corresponding author. The data are not publicly available due to an NDA and privacy.

**Conflicts of Interest:** The authors declare no conflicts of interest. The funders had no role in the design of the study; in the collection, analyses, or interpretation of data; in the writing of the manuscript; or in the decision to publish the results.

## References

1. Valbona, M.; Haghani, R.; Harryson, P. Bridge decks of fibre reinforced polymer (FRP): A sustainable solution. *Constr. Build. Mater.* **2014**, *50*, 190–199. [CrossRef]

2. Stankiewicz, B. Composite GFRP deck for bridge structures. *Procedia Eng.* **2012**, *40*, 423–427. [CrossRef]
3. Kim, Y.J. State of the practice of FRP composites in highway bridges. *Eng. Struct.* **2019**, *179*, 1–8. [CrossRef]
4. Vovesný, M.; Rotter, T. GFRP bridge deck panel. *Procedia Eng.* **2012**, *40*, 492–497. [CrossRef]
5. Ali, H.T.; Akrami, R.; Fotouhi, S.; Bodaghi, M.; Saeedifar, M.; Yusuf, M.; Fotouhi, M. Fiber reinforced polymer composites in bridge industry. *Structures* **2021**, *30*, 774–785. [CrossRef]
6. Qureshi, J. A Review of Fibre Reinforced Polymer Bridges. *Fibers* **2023**, *11*, 40. [CrossRef]
7. Siwowski, T.; Rajchel, M. A Polish approach to FRP bridges. *Sel. Sci. Pap. J. Civ. Eng.* **2017**, *12*, 47–54. [CrossRef]
8. Smits, J. Fiber-Reinforced Polymer Bridge Design in the Netherlands: Architectural Challenges toward Innovative, Sustainable, and Durable Bridges. *Engineering* **2016**, *2*, 518–527. [CrossRef]
9. Canning, L.; Luke, S. Development of FRP Bridges in the UK—An Overview. *Adv. Struct. Eng.* **2010**, *13*, 823–835. [CrossRef]
10. *EN 1990:2002*; Basis of Structural Design. European Committee For Standardization: Brussels, Belgium, 2011; Volume 1.
11. De Corte, W.; Uyttersprot, J.; Somers, R. FRP bridges in the Flanders region: Experiences from the C-bridge project. *Appl. Sci.* **2020**, *12*, 10897. [CrossRef]
12. De Corte, W.; Jansseune, A.; Van Paepegem, W.; Peeters, J. Elastic properties and failure behavior of tiled laminate composites. *Key Eng. Mater.* **2018**, *774*, 564–569. [CrossRef]
13. De Corte, W.; Jansseune, A.; Van Paepegem, W.; Peeters, J. Structural behaviour and robustness assessment of an InfraCore® inside bridge deck specimen subjected to static and dynamic local loading. *ICCM Int. Conf. Compos. Mater.* **2017**, *2017*, 20–25.
14. Uyttersprot, J.; De Corte, W.; Ingelbinck, B. Influence of SLS design requirements on the material consumption and self-weight of web-core sandwich panel FRP composite footbridges. *Compos. Struct.* **2021**, *262*, 18. [CrossRef]
15. FiberCore Europe. Portfolio FiberCore Europe. 2020. Available online: https://issuu.com/fibercore-europe/docs/fce_portfolio_brochure_2020_1000bruggen (accessed on 12 December 2024).
16. Karpenko, O.; Peeters, T.; Gommers, E.; White, T.; Tromp, L.; Pavlović, M. A Study On Fatigue Resistance And Structural Integrity. In *Web-Core Composite Bridge Deck Panels, Proceedings of the 21st European Conference on Composite Materials, Volume 3—Material and Structural Behavior—Simulation & Testing, Nantes, France, 2–5 July 2024*; La Cité Nantes Events Center: Nantes, France, 2024; pp. 1018–1025.
17. Siwowski, T.; Kaleta, D.; Rajchel, M. Structural behaviour of an all-composite road bridge. *Compos. Struct.* **2018**, *192*, 555–567. [CrossRef]
18. Abbood, I.S.; Odaa, S.A.; Hasan, K.F.; Jasim, M.A. Properties evaluation of fiber reinforced polymers and their constituent materials used in structures—A review. *Mater. Today Proc.* **2021**, *43*, 1003–1008. [CrossRef]
19. Aref, A.J.; Alampalli, S.; He, Y. Performance of a fiber reinforced polymer web core skew bridge superstructure. Part. II: Failure modes and parametric study. *Compos. Struct.* **2005**, *69*, 500–509. [CrossRef]
20. Davids, W.G.; Diba, A.; Dagher, H.J.; Guzzi, D.; Schanck, A.P. Development, assessment and implementation of a novel FRP composite girder bridge. *Constr. Build. Mater.* **2022**, *340*, 127818. [CrossRef]
21. Burhan, I.; Kim, H.S. S-n curve models for composite materials characterisation: An evaluative review. *J. Compos. Sci.* **2018**, *2*, 38. [CrossRef]
22. Alagusundaramoorthy, P.; Veera Sudarsana Reddy, R. Testing and evaluation of GFRP composite deck panels. *Ocean Eng.* **2008**, *35*, 287–293. [CrossRef]
23. Hiddingh, J.; Grefhorst, R.; Veltkamp, M. Full-scale fatigue testing with initial damage as validation of FRP road bridge design. In *IABSE Congress Stockholm, 2016: Challenges in Design and Construction of an Innovative and Sustainable Built Environment*; IABSE: Zurich, Switzerland, 2016; pp. 1280–1287. [CrossRef]
24. Shahkhosravi, N.A.; Yousefi, J.; Najafabadi, M.A.; Burvill, C.; Minak, G. Fatigue life reduction of GFRP composites due to delamination associated with the introduction of functional discontinuities. *Compos. Part B Eng.* **2019**, *163*, 536–547. [CrossRef]
25. *ASTM D7264*; Standard Test Method for Flexural Properties of Polymer Matrix Composite Materials. ASTM: West Conshohocken, PA, USA, 2011.
26. Van Der Steen, C. *CUR96:2019*; Vezelversterkte Kunststoffen in Bouwkundige en Civieltechnische Draagconstructies—In Dutch; CROW: Delft, The Netherlands, 2019.
27. Heinemeyer, C.; Butz, C.; Keil, A.; Schlaich, M.; Goldbeck, A.; Trometor, S.; Lukic, M.; Chabrolin, B.; Lemaire, A.; Martin, P.; et al. *JRC Scientific and Technical Reports—EUR 23984 EN: Design of Lightweight Footbridges for Human. Induced Vibrations*; European Commission—Joint Research Centre: Aachen, Germany, 2009. [CrossRef]
28. Instron. 8801 Servohydraulic Fatigue Testing System. n.d. Available online: https://www.instron.com/-/media/literature-library/products/2013/10/8801-fatigue-testing-system.pdf (accessed on 12 December 2024).